Modeling and Control of Shape Memory Alloy Actuators

J. Jayender, *Student Member, IEEE*, R. V. Patel, *Fellow, IEEE*, S. Nikumb, and M. Ostojic, *Member, IEEE*

***Abstract*—This brief describes a new model for shape memory alloy (SMA) actuators based on the physics of the process and develops control strategies using the model. The model consists of three equations—the temperature dynamics described by Joules heating-convectional cooling, the mole fraction distribution with temperature given by statistics to describe a two state system, and a constitutive equation relating the changes in temperature and mole fraction to the stress and strain induced in the SMA. This model is used to develop two control schemes for controlling the strain in an SMA actuator. The first control scheme describes a gain-scheduled proportional–integral (PI) controller, the gains of which are obtained by means of linear quadratic regulator (LQR) optimization. The second control scheme is an $\mathcal{H}_\infty$ loop-shaping controller using normalized coprime stabilization which ensures robust stability by minimizing the effect of unmodeled dynamics at high frequencies. Simulation and experimental results show fast and accurate control of the strain in the SMA actuator for both control schemes.**

***Index Terms*—Fermi–Dirac principle, gain scheduling, linear quadratic regulator (LQR) optimization, robust loop-shaping H-infinity controller, shape memory alloy (SMA).**

I. Introduction

THERE HAS been of considerable interest in recent years in developing shape memory alloy (SMA) actuators because of their advantages in producing large plastic deformations, high power-to-weight ratio and low driving voltages. These advantages coupled with the fact that SMAs are biocompatible make them good candidates for medical applications where the workspace is compact. Some applications of SMA actuators in the biomedical field are medical forceps [1], [2], vascular stents, instruments for minimally invasive therapy [3], active catheters [4], [5], artificial muscle [6], etc. SMA actuators have also found applications in robotics [7]–[9], vibration control [10], and active control of space structures [11] due to their ability to generate high forces. However, the main disadvantage of an SMA actuator is the nonlinear response of the strain to input current. SMAs demonstrate a hysteresis characteristic as a result of which their control is imprecise and difficult. The efficiency of an SMA actuator depends on the accuracy of its control, which in turn depends on the mathematical model of the SMA.

Manuscript received January 6, 2007. Manuscript received in final form April 12, 2007. Recommended by Associate Editor R. Rajamani. This work was supported in part by the Natural Sciences and Engineering Research Council (NSERC) of Canada under Grant RGPIN-1345 and by the Canada Foundation for Innovation under an infrastructure grant.

J. Jayender and R. V. Patel are with the University of Western Ontario, London, ON N6A 5B9 Canada (e-mail: jjagadee@uwo.ca, rajni@eng.uwo.ca)

S. Nikumb and M. Ostojic are with the Integrated Manufacturing Technologies Institute (IMTI), National Research Council (NRC), London, ON N6G 4X8 Canada (e-mail: suwas.nikumb@nrc.gc.ca; mile.ostojic@nrc.gc.ca).

Digital Object Identifier 10.1109/TCST.2007.903391

There have been quite a few papers on modeling and control of SMA behavior. Most models use a curve-fitting-based method to develop a mathematical description of the SMA and use the dynamic equations thus obtained to control it. A continuous-time model, developed by Arai *et al.* [12] fits a differential equation to experimental data. This model, however, is not based on the actual physical process involved and the performance cannot be guaranteed over the entire operating region.

The Preisach model has also been used to model the hysteresis of the SMA [13]–[16]. Although this model explains the hysteresis characteristic and the minor loops, the formulation is based on experimental data and not on the actual process. This model is also not convenient for developing control strategies. Models based on experimental data cannot guarantee robust performance and stability under all operating conditions. The model becomes inaccurate if the SMA actuator operates in an environment other than air, in which the experimental data was obtained.

Fixed gain proportional–integral–differential (PID) control does not work well since the SMA demonstrates a highly nonlinear behavior. Feedback linearization has been used to varying degrees of success [8], [17]. The problem with feedback linearization is that it depends on accurate cancellation of the nonlinear components of the SMA response which in turn depends on a number of parameters and the accuracy of the model. In order to overcome these problems, variable structure control has been utilized since the control strategy is fairly insensitive to uncertainties in the parameters of the model [18], [19]. However, the problem with variable structure control is that tracking is possible so long as the error is small. The discontinuous nature of switching may also introduce ringing and excite high frequency components in the system which are not desirable.

In this brief, we present a model for the SMA behavior based on the physical process involved. This model consists of three dynamic equations describing the variation of mole fraction with temperature using Fermi–Dirac statistics, temperature dynamics based on Joules heating—convectional cooling, and a constitutive equation relating the stress and strain in SMA to changes in temperature and the mole fraction of the SMA in the Austenite phase. The advantage of the proposed model is that it does not depend on experimental behavior of the SMA and can also accurately describe its behavior in fluids such as water and blood.

This model is written in state-space form in order to develop the control strategies. Two control schemes have been developed—a gain-scheduled PI controller, the gains of which are obtained from LQR optimization and an $\mathcal{H}_\infty$ loop-shaping controller using normalized coprime stabilization.

Section II explains the model developed for the SMA. Section III describes the experimental setup for validating the control schemes. No-load simulation and experimental results are compared in Section IV. The dynamic equations

representing the model are written in state-space form in Section V. Section VI deals with the LQR controller design and presents simulation and experimental results for the controller. Section VII describes the $\mathcal{H}_\infty$ loop-shaping controller and presents the corresponding simulation and experimental results and, finally, Section VIII gives some concluding remarks.

II. Theory and Modeling

The model consists of three equations.

A. Modeling of Phase Transformation

Since an SMA exists only in Martensite and Austenite phases, it can be modeled as a two-state system, like an electron. The Fermi–Dirac statistics, which describe the distribution of electrons in two states depending on their energy levels, has been found to provide a good model for the state of an SMA in Martensite and Austenite forms.

We use two modeling equations based on whether the alloy is being heated or cooled due to hysteresis with two different transition temperatures. Since the SMA is in the Martensite form at lower temperatures, the phase transformation equation during heating is described by analogy with the Fermi–Dirac statistics in the form

$$\xi = \frac{\xi_m}{1 + \exp\left(\frac{T_{f_a} - T}{\sigma_a} + K_a\sigma\right)} \tag{1}$$

where ξ is the fraction of the Austenite phase, ξ_m is the fraction of the Martensite phase prior to the present transformation from Martensite to Austenite, T is the temperature, T_{f_a} is the transition temperature from Martensite to Austenite, σ_a is an indication of the range of temperature around the transition temperature T_{f_a} during which the phase change occurs, σ is the stress, and K_a is the stress curve-fitting parameter which is obtained from the loading plateau of the stress-strain characteristic with no change in temperature.

On cooling, the Austenite phase gets converted to the Martensite phase and the modeling equation during cooling is described by analogy with the Fermi–Dirac statistics in the form

$$\xi = \frac{\xi_a}{1 + \exp\left(\frac{T_{f_m} - T}{\sigma_m} + K_m\sigma\right)} \tag{2}$$

where ξ_a is the fraction of the Austenite phase prior to the present transformation from Austenite to Martensite, T is the temperature, T_{f_m} is the transition temperature from Austenite to Martensite, σ_m is an indication of the range of temperature around the transition temperature T_{f_m} during which the phase change occurs, σ is the stress, and K_m is the stress curve-fitting parameter which is obtained from the unloading part of the stress-strain characteristic. The parameters K_a and K_m indicate the response of the SMA to application of external stress. This model includes both twinned and detwinned Martensite phases. Since the SMA is modeled as a two-component system, at any given time, the sum of the mole fractions of the Austenite and Martensite phase is 1, i.e.,

$$\xi_a + \xi_m = 1. \tag{3}$$

The time derivatives of (1) and (2) are as follows.

For heating

$$\dot{\xi} = \frac{\xi^2}{\xi_m}\left[\exp\left(\frac{T_{f_a} - T}{\sigma_a} + K_a\sigma\right)\right]\left[\frac{\dot{T}}{\sigma_a} - K_a\dot{\sigma}\right]. \tag{4}$$

For cooling

$$\dot{\xi} = \frac{\xi^2}{\xi_a}\left[\exp\left(\frac{T_{f_m} - T}{\sigma_m} + K_m\sigma\right)\right]\left[\frac{\dot{T}}{\sigma_m} - K_m\dot{\sigma}\right]. \tag{5}$$

B. Modeling of Temperature Dynamics

The SMA actuator is heated by the process of Joules heating by applying a voltage across the SMA. The loss of heat from the SMA is through natural convection. Mathematically the dynamics of the temperature are given by the following equation which has also been used in [18]

$$\dot{T} = \frac{1}{mc_p}\left[\frac{V^2}{R} - hA(T - T_a)\right] \tag{6}$$

where m is the mass per unit length, c_p is the specific heat capacity, V is the voltage applied across the SMA, R is the resistance per unit length, h is the coefficient of convectional cooling, $A = \pi d$ is the circumferential area of cooling, d is the diameter of the wire, T is the temperature, and T_a is the ambient temperature. The coefficient h is assumed to have the characteristics of a second-order polynomial to enhance the rate of convection at higher temperatures as observed in open-loop results

$$h = h_0 + h_2T^2. \tag{7}$$

C. Constitutive Equation

The constitutive equation relating changes in stress, strain, temperature, and mole fraction is given by the following equation and has been previously used in [18]:

$$\dot{\sigma} = D\dot{\epsilon} + \theta_t\dot{T} + \Omega\dot{\xi} \tag{8}$$

where σ is the stress in the SMA, D is the Young's modulus of the alloy, ϵ is the strain, θ_t is the thermal expansion factor, $\Omega = -D\epsilon_i$ is the phase transformation contribution factor, and ϵ_i is the initial strain in the SMA. The model is capable of explaining the shape memory and super-elastic properties of Ni-Ti alloys. It should be noted here that in (8), D can be assumed to be the average of the Young's moduli for the Martensite and Austenite phases to model the shape memory effect while a more precise Young's modulus based on the composition of

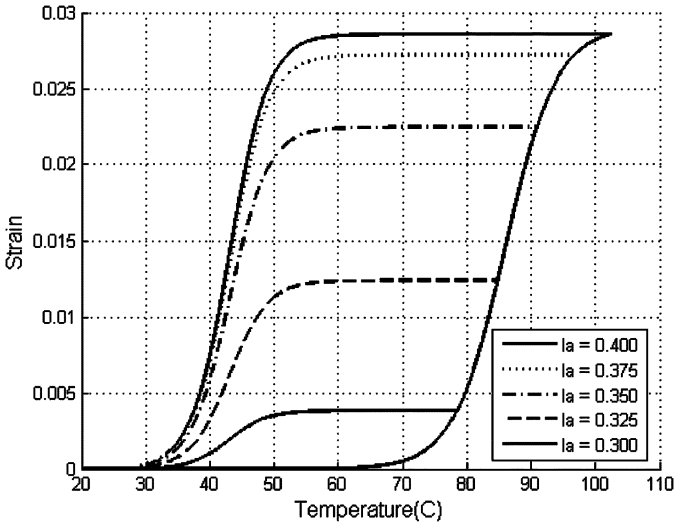

Fig. 1. Hysteresis characteristics of SMA for varying sinusoidal input.

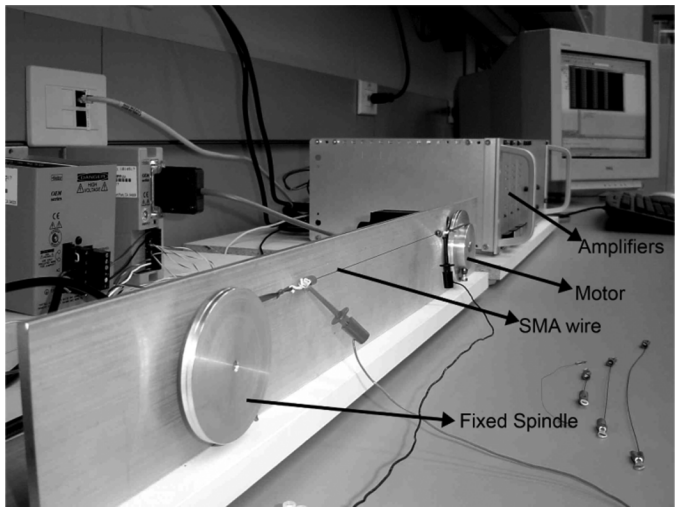

Fig. 2. Experimental setup.

TABLE I
PARAMETERS OF THE SMA

Parameter	Value
Mass per unit length (m in $kg.m^{-1}$)	$4.54e^{-4}$
Specific heat capacity (c_p in $J.kg^{-1}.K^{-1}$)	320
Resistance per unit length (R in $\Omega.m^{-1}$)	13.0677
Young's Modulus(Austenite) (D_a in $N.m^{-2}$)	$75e^{9}$
Young's Modulus(Martensite) (D_m in $N.m^{-2}$)	$28e^{9}$
Thermal Expansion (θ_t in $N.m^{-2}.K^{-1}$)	$-11e^{-6}$
SMA initial strain (ϵ_i)	0.03090
Heat convection coefficient (h_0 in $J.m^{-2}.s^{-1}.K^{-1}$)	28.552
Heat convection coefficient (h_2 in $J.m^{-2}.s^{-1}.K^{-3}$)	$4.060e^{-4}$
Diameter of wire (in m)	$304e^{-6}$
Length of wire (in m)	0.24
Ambient temperature (T_a in ^oC)	20
Martensite to Austenite transformation temperature (T_{f_a} in ^oC)	85
Austenite to Martensite transformation temperature (T_{f_m} in ^oC)	42
Spread of temperature around T_{f_a} (σ_a in ^oC)	6
Spread of temperature around T_{f_m} (σ_m in ^oC)	4.5

the alloy would be required to model the super-elastic property. This brief, however, deals only with the shape memory effect of Ni-Ti alloys.

The model also explains the hysteresis as well as the minor loops in the hysteresis, as illustrated in Fig. 1. In addition, the experimental results obtained for the control of the SMA actuator further justify the model since an accurate model is crucial for obtaining good results. The parameters of the model are listed in Table I.

III. EXPERIMENTAL SETUP

In the experimental setup, the SMA wire is attached between a fixed support and a motor which provides a constant tension to keep the wire taut at all times. The readings from the encoder of the motor give the change in strain in the SMA wire which is fed to a computer through an input/output (I/O) card. The real-time implementation of the controller was done in C++ on a Windows-based PC. The setup is shown in Fig. 2. For the experiments on the SMA actuator in water, the setup is modified such that the SMA wire is completely immersed in water and one end of the SMA is attached to the motor to create tension in the wire.

IV. STATE-SPACE REPRESENTATION

The dynamic characteristics of the SMA are completely defined by (4) or (5) (heating or cooling), together with (6) and (8). We can also define σ_e as the integral of the error, i.e.,

$$\dot{\sigma_e} = \epsilon - \epsilon_{\text{ref}} \tag{9}$$

where ϵ is the strain of the SMA actuator and ϵ_{ref} is the reference trajectory. The dynamic equations of the SMA along with (9) can be represented in the state-space form

$$\dot{\bar{z}} = f(\bar{z}, u, t) \tag{10}$$

where

$$\bar{z} = \begin{bmatrix} \epsilon & T & \xi & \sigma_e \end{bmatrix}^T$$

and u is the input voltage to the SMA wire. The nonlinear equations are linearized about a set of operating points $(\epsilon_0, T_0, \xi_0, u_0)$ on the reference trajectory.

To obtain the operating points, ϵ_0 is chosen as the value of the reference strain at that instant of time. T_0 and ξ_0 are obtained by integrating (4) or (5) and (8), depending on whether the SMA is being heated or cooled, for a given value of ϵ_0. The value of u_0 is obtained from (6) for a given value of T_0, assuming steady-state conditions.

Equation (10) is linearized about the calculated operating points, assuming the no-load case, to obtain linear models in the form

$$\dot{\bar{z}} = \mathbf{A}\bar{z} + \mathbf{B}u, \quad y = \mathbf{C}\bar{z} \tag{11}$$

where

$$\mathbf{A} = \left[\frac{\partial f}{\partial \bar{z}}\right]_{\epsilon_0, T_0, \xi_0, u_0} \quad \mathbf{B} = \left[\frac{\partial f}{\partial u}\right]_{\epsilon_0, T_0, \xi_0, u_0}.$$

The closed form expressions of $\mathbf{A}$ and $\mathbf{B}$ are given as

$$\mathbf{A} = \begin{bmatrix} 0 & \frac{1}{D}H_{\text{func}}(-\theta_t - \Omega G_{\text{func}}) & 0 & 0 \\ 0 & H_{\text{func}} & 0 & 0 \\ 0 & H_{\text{func}}G_{\text{func}} & 0 & 0 \\ 1 & 0 & 0 & 0 \end{bmatrix}_{\epsilon_0, T_0, \xi_0, u_0}$$

$$\mathbf{B} = \begin{bmatrix} \frac{2u}{mc_pRD}(-\theta_T - \Omega G_{\text{func}}) \\ \frac{2u}{mc_pR} \\ \frac{2u}{mc_p}G_{\text{func}} \\ 0 \end{bmatrix}_{\epsilon_0, T_0, \xi_0, u_0}$$

where

$$H_{\text{func}} = \frac{-hA - 2h_2AT(T - T_a)}{mc_p} \tag{12}$$

$$G_{\text{func}} = \frac{K\exp(\frac{(T_f - T)}{\sigma_i})}{\sigma_i(1 + \exp(\frac{T_f - T}{\sigma_i}))^2} \tag{13}$$

where T_f is chosen either as T_{f_a} or T_{f_m} according to whether the SMA actuator is being heated or cooled. Correspondingly, σ_i is chosen as either σ_m or σ_a and K is chosen as ξ_m or ξ_a.

For the no-load case, which is the case considered here, σ and $\dot{\sigma}$ are equal to zero. In this case, the model given by (11) is not controllable since the number of controllable states is only 2. Physically, for a given input current, the SMA reaches a desired temperature resulting in a phase transformation which causes a change in strain as given by the constitutive equation. The three states (temperature, mole fraction, strain) cannot be independently controlled to a desired value. On removing the uncontrollable modes, the following state-space model is obtained

$$\dot{\bar{x}} = \mathbf{A}'\bar{x} + \mathbf{B}'u \tag{14}$$

where

$$\bar{x} = \begin{bmatrix} \epsilon \\ \sigma_e \end{bmatrix}.$$

The model is evaluated every 100 ms and the corresponding gain matrix is calculated. Since the plant dynamics are comparatively slow, the linear models closely approximate the nonlinear dynamics of the SMA around every operating point implying that the nonlinear dynamics of the system are taken into account in the models.

V. Gain Scheduled Controller

For a gain-scheduled PI controller (see Fig. 3), the feedback is of the form

$$u = -K_P(\epsilon - \epsilon_{ref}) - K_I\sigma_e + u_0 \tag{15}$$

where K_P is the proportional gain and K_I is the integral gain. Writing $\mathbf{K} = [K_p \quad K_I]$, the gains are computed such that the resulting controller minimizes the quadratic cost function

$$\mathbf{J}(u) = \int_0^\infty (x^T\mathbf{Q}x + u^T\mathbf{R}u)\,dt. \tag{16}$$

The choice of gains for minimizing $\mathbf{J}(u)$ are obtained by first solving for $\mathbf{S}$ in the algebraic Riccati equation

$$\mathbf{A'}^T\mathbf{S} + \mathbf{S}\mathbf{A}' - \mathbf{S}\mathbf{B}'\mathbf{R}^{-1}\mathbf{B'}^T\mathbf{S} + \mathbf{Q} = 0. \tag{17}$$

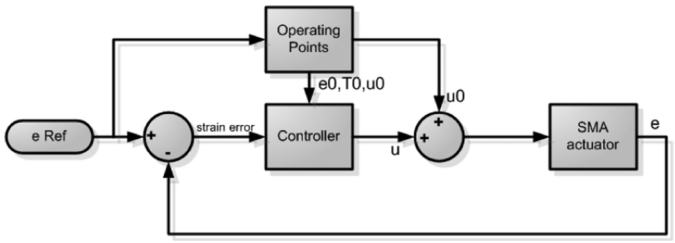

Fig. 3. Controller for the SMA actuator.

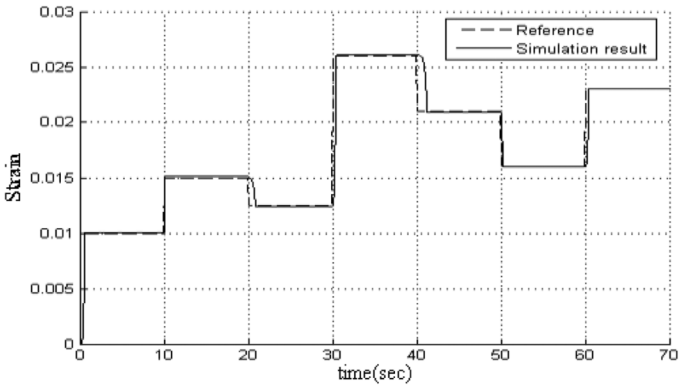

Fig. 4. Simulation results. Closed-loop SMA response to a step reference input.

The matrix $\mathbf{K}$ is given by

$$\mathbf{K} = \mathbf{R}^{-1}\mathbf{B'}^T\mathbf{S}. \tag{18}$$

1) Simulation and Experimental Results for Closed-Loop Control of SMA in Air: The simulation of the controller and SMA was done using MATLAB. The values of $\mathbf{Q}$ and $\mathbf{R}$ were chosen as

$$\mathbf{Q} = \texttt{diag}(7.2e^6, 500) \quad \mathbf{R} = 0.003.$$

The simulation results for an input consisting of step changes are shown in Fig. 4. Fig. 4 shows an accurate tracking of the step reference. The rate of heating of the SMA can be controlled while the rate of cooling of the SMA wire, which happens through natural convection, cannot be controlled. The simulation for a sinusoidal reference input results in an RMS error of 0.4% and a maximum error of 1.94% of the reference input, thereby confirming the good performance of the controller.

The strain of the SMA actuator, however, gets distorted when the reference changes too fast, as the rate of cooling is slow compared to the rate of heating and cannot be controlled to ensure a faster rate of cooling.

The experimental verification of the controller was done on a 700 MHz Windows-based PC at a sampling rate of 65 Hz. Since the forms of the matrices $\mathbf{A}'$ and $\mathbf{B}'$ are fairly simple, the solution for the Ricatti equation was obtained in closed form using MAPLE. This also greatly reduced the computation time by avoiding matrix computations such as the Schur decomposition [20]. The experimental closed-loop response of the SMA to step changes is shown in Fig. 5(a).

From the experimental results, it can be observed that the response time for heating is approximately 1.0 s and for cooling

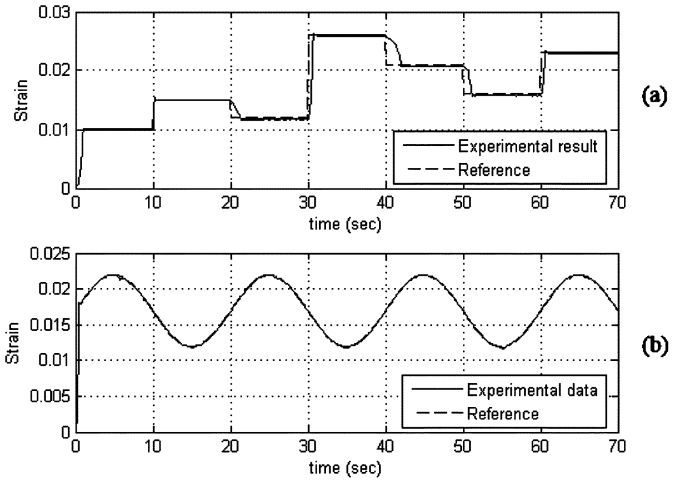

Fig. 5. Experimental result. (a) Closed-loop SMA response in air to step reference input. (b) Sinusoidal reference input.

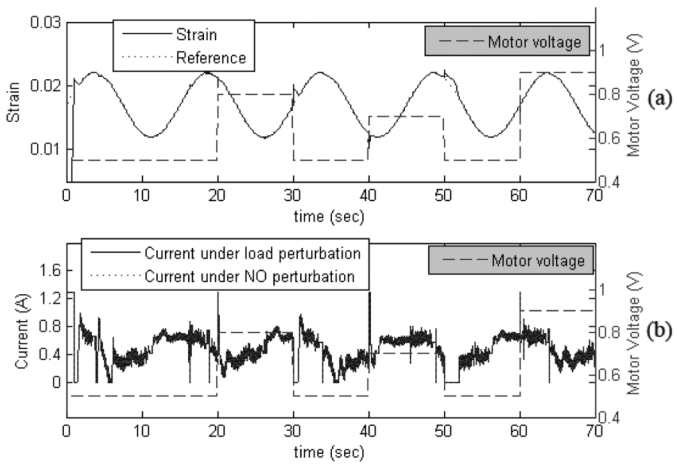

Fig. 6. Experimental results. (a) Closed-loop SMA response in the presence of load perturbations. (b) Controller output.

is 2.1 s for a 304 μm diameter SMA wire. The rate of cooling is much higher for a thinner wire since the ratio of surface area to volume increases as the wire diameter is reduced, thereby increasing the rate of convectional cooling.

The experimental results for a sinusoidal reference input are shown in Fig. 5(b) which shows an excellent tracking of the reference trajectory by the SMA in closed-loop. Neglecting the first 5 s of data until the strain in the SMA reaches the reference, the strain in the SMA tracks the reference with a maximum error of 3.14% and RMS error of 0.91%.

The dc offset and frequency of the reference were also varied to check the performance of the controller in the entire operating range. The controller has good performance over the entire operating range and for frequencies lower than 0.1 Hz.

2) Perturbations: An external load disturbance was applied to verify the performance of the controller. The load disturbance can be considered as an additive disturbance. The disturbance was introduced by increasing the input voltage to the motor causing tension in the SMA wire. The closed-loop response and the controller output in the presence of the load disturbance are shown in Fig. 6. The RMS error for tracking a sinusoidal reference is 2.63%, confirming the negligible effect of load disturbances on the plant. The results show that the LQR controller provides robust performance and stability in the presence of the load disturbances.

The performance of the controller was further verified by blowing air over the SMA wire. The external disturbance was created by placing a dc computer fan at a distance of 10 cm from the SMA wire. This caused an increase in the rate of cooling resulting in an increase in the coefficient of convectional cooling h. Therefore, this perturbation caused an uncertainty in the SMA model. The result for the controller performance and the input current to the SMA are shown in Fig. 7. The LQR controller provides robust stability while the performance is somewhat degraded, showing a steady-state error in the presence of the disturbance. The RMS error for tracking a sinusoidal reference is 1.69%. The degraded performance of the LQR controller in presence of cooling rate disturbance is further verified in liquids.

3) Experimental Verification of Controller in Liquids: Since the primary application of this work is for biomedical purposes,

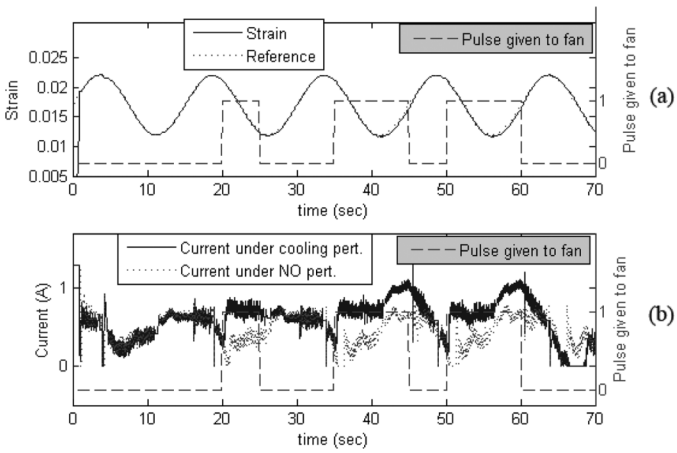

Fig. 7. Experimental results. (a) Closed-loop SMA response in the presence of perturbations in the cooling rate. (b) Controller output.

the performance of the LQR controller for the SMA actuator was also studied in liquids. For convenience, we chose to conduct the tests using water and milk. The coefficient of cooling h for the model was calculated by the formula given in [21]. The coefficient h for water was calculated to be 1156 $\mathrm{Jm^{-2}s^{-1}K^{-1}}$. The experimental results for closed-loop control of the SMA wire in water for a sinusoidal reference input is shown in Fig. 8. Neglecting the first 5 s of data until the strain in the SMA reaches the reference, the RMS error for tracking a sinusoidal input is 1.19%. The excellent closed-loop results obtained for the SMA actuator in water further validate the model since the LQR controller design depends on the accuracy of the model. Since the rate of cooling in water is higher than that in air, the controller shows good performance for operating frequencies up to 1 Hz.

Milk, like blood, is a mixture, containing suspended proteins akin to the red blood cells (RBC) and white blood cells (WBC) in blood. The performance of the SMA actuator in milk is a good indicator of the expected performance in blood. The response of the controller was also verified in the presence of perturbations caused by stirring milk at 138 r/min, as shown in Fig. 9. The RMS error for tracking the sinusoidal reference in

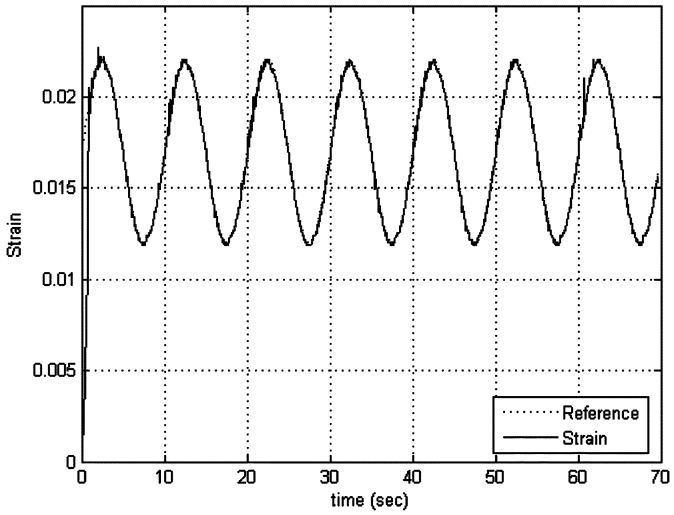

Fig. 8. Experimental result. Closed-loop SMA response to a sinusoidal reference input in water.

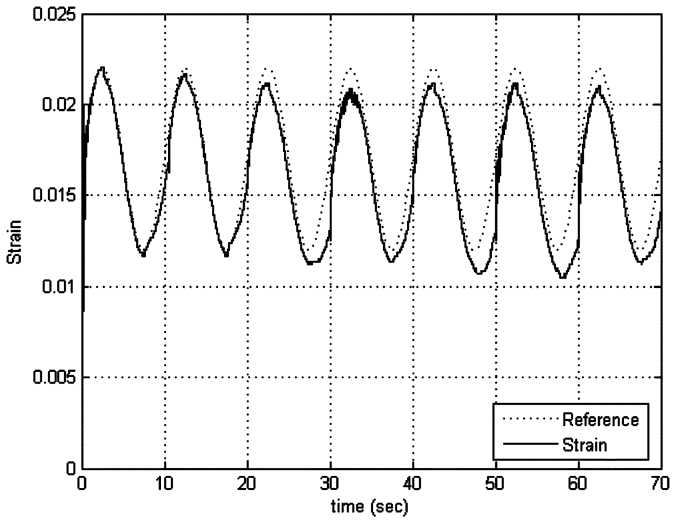

Fig. 9. Experimental result. Closed-loop SMA response to a sinusoidal reference input in milk in the presence of perturbation.

milk is 8.66%, thereby confirming the degraded performance in the presence of perturbations affecting the rate of cooling.

Remarks: The simulation and experimental results obtained clearly indicate the need for choosing proper gains for the controller given by (15). The LQR controller provides excellent tracking of step and sinusoidal input in air, water and milk in the absence of any perturbations. For load disturbances, the LQR controller provides good disturbance rejection and maintains robust stability and performance. However, the controller is sensitive to unmodelled dynamics at high frequencies which could lead to instability. In addition, perturbations in the cooling rate cause a significant steady-state error. The selection of gains for the PI controller is essential for good disturbance rejection. For this reason, an $\mathcal{H}_\infty$ loop-shaping controller using normalized coprime stabilization is designed to provide both robust stability and performance.

VI. Robust Controller

From Fig. 10, it is known that in order to reject disturbances (d and d_i) at the plant output y and control input u_p, the sensitivity

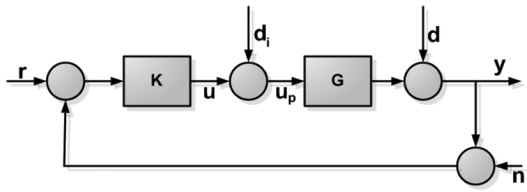

Fig. 10. Standard feedback with disturbance and noise.

function S, defined by,

$$S = (1 + GK)^{-1}$$

should be minimized (or the loop gain of GK should be maximized) at the frequencies where the disturbance is dominant [22]. However, the loop gains cannot be made arbitrarily large over a large frequency range. High loop gains in the frequency range where the model is uncertain could lead to instability. Therefore, the robust controller is designed such that the gains are high when the model describes the SMA accurately and low at higher frequencies when the model is inaccurate, thereby suppressing the unmodeled dynamics at higher frequencies.

The gain matrix $\mathbf{K} = [K_p \quad K_I]$ of the PI controller, as given by (15), is computed by the loop-shaping procedure using normalized coprime stabilization [23], [24]. The nominal plant G(SMA) is first shaped by using a precompensator W_1 so that the singular values of the nominal plant G are shaped to a desired open-loop shape. The compensator also ensures that the shaped plant $G_s = GW_1$ is square and G_s has no hidden modes.

For ensuring robust stabilization, $\epsilon_{\max}$ is calculated as

$$\epsilon_{\max} = \left(\inf_{K \text{stabilizing}} \left\| \begin{bmatrix} I \\ K \end{bmatrix} (I + G_s K)^{-1} \tilde{M}_s^{-1} \right\|_\infty \right)^{-1} \tag{19}$$

$$= \sqrt{1 - \| [\tilde{N}_s \quad \tilde{M}_s] \|_H^2} \tag{20}$$

where $\tilde{M}_s$ and $\tilde{N}_s$ define the normalized coprime factors of G_s. An $\epsilon \leq \epsilon_{\max}$ is selected to form a stabilizing controller K_∞, which satisfies

$$\left\| \begin{bmatrix} I \\ K_\infty \end{bmatrix} (I + G_s K_\infty)^{-1} \tilde{M}_s^{-1} \right\|_\infty \leq \epsilon^{-1} \doteq \gamma. \tag{21}$$

The final feedback controller K is obtained as the product of the precompensator W_1 and the $\mathcal{H}_\infty$ controller K_∞, i.e.,

$$K = W_1 K_\infty. \tag{22}$$

1) Simulation and Experimental Results for Closed-Loop Control of SMA in Air: The desired loop shape was chosen so that the gains are high at low frequencies where the model describes the SMA accurately and the gains roll off at -20 dB/decade beyond the corner frequency, thereby ensuring a low gain at high frequencies. The open loop-shaping transfer function was chosen to be

$$G_d(s) = \frac{\omega_0}{s} \tag{23}$$

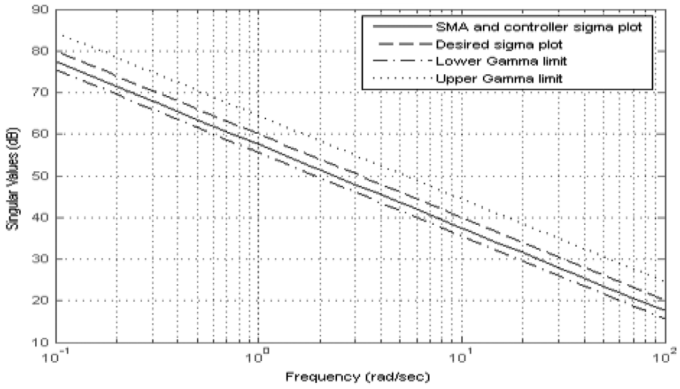

Fig. 11. Singular value plot of the open-loop SMA and controller transfer function.

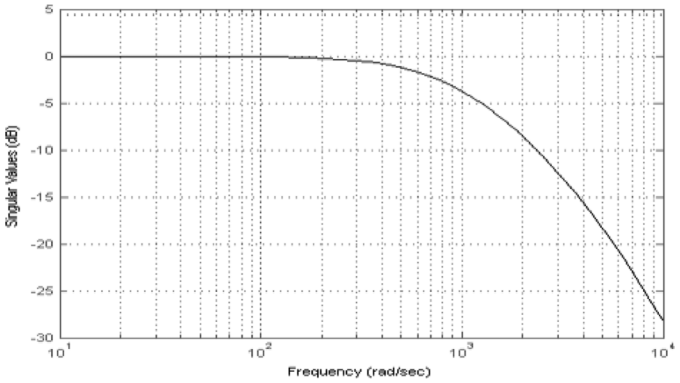

Fig. 12. Singular value plot of the closed-loop SMA and controller transfer function.

where ω_0 is the corner frequency. A stabilizing $\mathcal{H}_\infty$ controller was computed to shape the singular value plot of $G(j\omega)K(j\omega)$ to have a desired loop shape $G_d(j\omega)$ with accuracy γ such that

$$|G(j\omega)K(j\omega)| \geq \frac{1}{\gamma}|G_d(j\omega)|, \qquad \text{for}\,\omega < \omega_0 \tag{24}$$

$$|G(j\omega)K(j\omega)| \leq \frac{1}{\gamma}|G_d(j\omega)|, \qquad \text{for}\,\omega > \omega_0. \tag{25}$$

The value of the corner frequency was chosen to be 1000.4 rad/s^{-1} to enable good tracking of the reference and disturbance rejection in a large frequency range. The singular value plot of $G(j\omega)K(j\omega)$ is shown in Fig. 11 and the closed-loop plot is shown in Fig. 12. However, it was observed that by choosing the corner frequency to be 1000.4 rad/s^{-1} the controller output saturated. Therefore, in order to obtain the benefits of good disturbance rejection, minimal tracking error and avoiding actuator saturation, the corner frequency was chosen to be 10.4 rad/s^{-1} for the first 200 ms until the error is small, thereafter the corner frequency is chosen to be 1000.4 rad/s^{-1}. In both regions of operation, robust stability can be assured without saturating the actuators.

The simulation to verify the controller design was done using MATLAB. For a sinusoidal reference input, the strain in the SMA actuator tracks the reference with a maximum error of 1.48% and an RMS error of 0.29%. The simulation, therefore, illustrates excellent tracking of the reference input and validates the controller design.

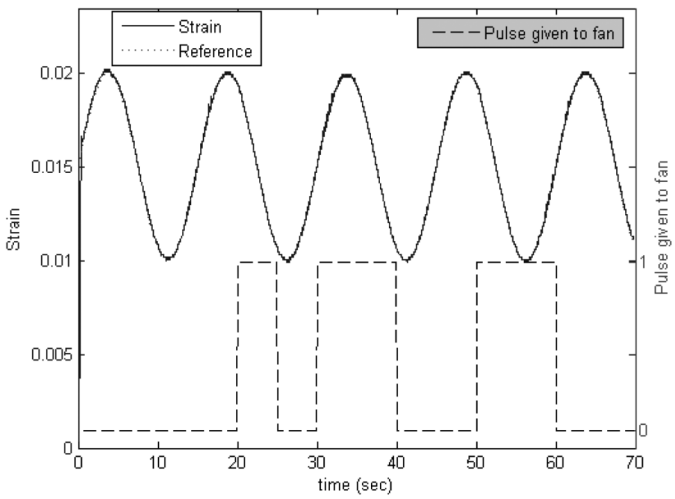

Fig. 13. Experimental results. Closed-loop SMA response to a sinusoidal reference input in presence of perturbation in the cooling rate.

Experimental verification of the controller was done on a 700-MHz Windows-based PC at a sampling rate of 100 Hz. For a sinusoidal reference input, the strain in the SMA tracks the reference with a maximum error of 2.62% and RMS error of 0.73%, neglecting the first five seconds of data until the strain in the SMA reaches the reference. The experimental results are comparable with the results obtained for the LQR controller in the absence of any perturbation in air, showing accurate tracking of the reference trajectories.

2) Perturbations: The performance of the robust controller was verified by applying a load disturbance to the SMA actuator. The performance of the controller is similar to the LQR controller and tracks the sinusoidal reference with an RMS error of 2.78%. The controller maintains robust stability and performance in the presence of load disturbances.

Another disturbance was applied to the SMA actuator by blowing air over the SMA wire. The closed-loop tracking of the sinusoidal reference in the presence of the disturbance is shown in Fig. 13. Unlike the LQR controller, the robust controller provides excellent performance in addition to robust stability. The sinusoidal trajectory is tracked with negligible steady-state error of RMS value 1.03% in the presence of the disturbance.

3) Experimental Verification of Controller in Liquids: The closed-loop control of the SMA actuator was also verified in liquids (water and milk). The results for the sinusoidal tracking of strain in the SMA actuator operating in water is given in Fig. 14. The RMS error for closed-loop tracking of a sinusoidal reference input in water is 1.21%, neglecting the first 5 s of data. Fig. 14 shows excellent tracking of the sinusoidal reference trajectory in liquids. In addition, the controller performance was verified in the presence of perturbations caused by stirring the liquid at 138 r/min, as shown in Fig. 15. Fig. 15 shows far better performance than that for the LQR controller (shown in Fig. 9). The robust controller provides excellent disturbance rejection.

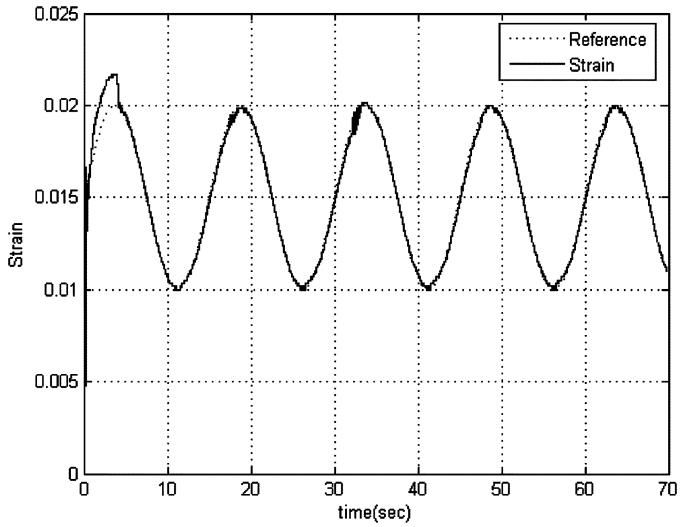

Fig. 14. Experimental results. Closed-loop SMA response to a sinusoidal reference input in water.

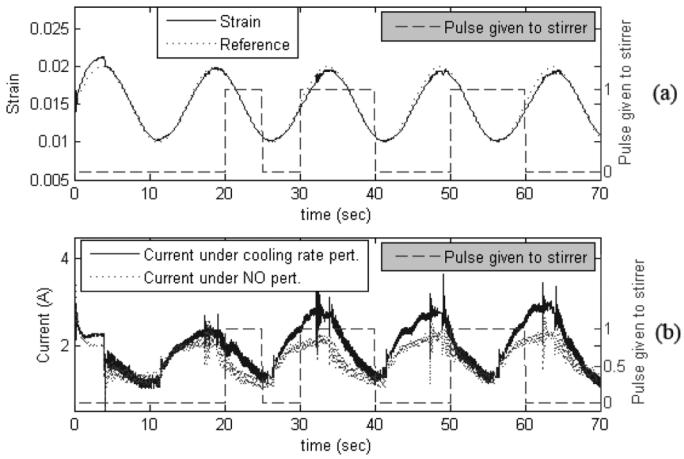

Fig. 15. Experimental results. (a) Closed-loop SMA response to a sinusoidal reference input in milk in presence of perturbation. (b) Controller output.

The sinusoidal trajectory is tracked with a steady-state RMS error value of 2.69%.

VII. Conclusion

In this brief, we have developed a new model for SMA actuators based on the physics of the process where we have used the Fermi–Dirac statistical model to represent the two-state process. Based on this model, we have developed and implemented experimentally two controllers: a gain-scheduled controller based on LQR optimization and an $\mathcal{H}_\infty$ loop-shaping controller. The simulation and experimental results in the absence of perturbations show excellent tracking response for the SMA, thereby validating both the model and the control scheme. In particular, the results also clearly justify the use of the model for describing the transformation between Martensite and Austenite phases. The controllers have the ability to reject uncertainties in the parameters of the model. However, it was observed experimentally that the $\mathcal{H}_\infty$ loop-shaping controller performed better than the LQR controller in the presence of perturbations, as shown in Table II. The high accuracy achieved by the controllers makes it possible to use SMA actuators safely for critical applications such as in biomedical devices and tools.

TABLE II
RMS Error (%) for Two Control Schemes

	LQR control	$\mathcal{H}_\infty$ control
Simulation results		
No pert. (Air)	0.40	0.29
Experimental results		
No pert. (Air)	0.91	0.73
Load pert. (Air)	2.63	2.78
Cooling-rate pert. (Air)	1.69	1.03
No pert. (Water)	1.19	1.21
Cooling-rate pert. (Milk)	8.66	2.69

References

[1] M. Hashimoto, T. Tabata, and T. Yuki, "Development of electrically heated SMA active forceps for laparoscopic surgery," in *Proc. IEEE Int. Conf. Robot. Autom.*, 1999, pp. 2372–2377.
[2] Y. Nakamura, A. Matsui, T. Saito, and K. Yoshimoto, "Shape-memory-alloy active forceps for laparoscopic surgery," in *Proc. IEEE Int. Conf. Robot. Autom.*, 1995, pp. 2320–2327.
[3] S. Payandeh, J. Rothe, and A. Parameswaran, "Design and development of actuating system for diagnostics application in minimally invasive surgery (MIS)," in *Proc. 23rd Ann. Int. Conf. IEEE Eng. Med. Bio. Soc.*, 2001, pp. 3473–3476.
[4] Y. Haga, Y. Tanahashi, and M. Esashi, "Small diameter active catheter using Shape Memory Alloy," in *Proc. 11th Ann. Int. Workshop Micro Electro Mech. Syst.*, 1998, pp. 419–424.
[5] S. Maeda, K. Abe, K. Yamamoto, O. Tohyama, and H. Ito, "Active endoscope with SMA (shape memory alloy) coil springs," in *Proc. 9th Ann. Int. Workshop Micro Electro Mech. Syst.*, 1996, pp. 290–295.
[6] J. Madden, N. Vandesteeg, P. Anquetil, P. Madden, A. Takshi, R. Pytel, S. Lafontaine, P. Wieringa, and I. Hunter, "Artificial muscle technology: Physical principles and naval prospects," *IEEE J. Ocean. Eng.*, vol. 29, no. 7, pp. 706–728, Jul. 2004.
[7] C. Pfeiffer, K. DeLaurentis, and C. Mavroidis, "Shape memory alloy actuated robot prostheses: Initial experiments," in *Proc. IEEE Int. Conf. Robot. Autom.*, 1999, pp. 2385–2391.
[8] M. Moallem and J. Lu, "Application of shape memory alloy actuators for flexure control: Theory and experiments," *IEEE/ASME Trans. Mechatronics*, vol. 10, no. 5, pp. 495–501, Oct. 2005.
[9] K.-Y. Tu, T.-T. Lee, C.-H. Wang, and C.-A. Chang, "Design of fuzzy walking pattern (FWP) for a shape memory alloy (SMA) biped robot," in *Proc. IEEE Int. Conf. Syst., Man, Cybern.*, 1998, pp. 3266–3271.
[10] S. Saadat, J. Salichs, M. Noori, Z. Hou, H. Davoodi, I. Bar-on, Y. Suzuki, and A. Masuda, "An overview of vibration and seismic applications of NiTi shape memory alloy," *Smart Mater. Structures*, vol. 11, pp. 218–229, 2002.
[11] F. Peng, X.-X. Jiang, Y.-R. Hu, and A. Ng, "Application of shape memory alloy actuators in active shape control of inflatable space structures," in *Proc. IEEE Conf. Aerosp.*, 2005, pp. 1–10.
[12] K. Arai, S. Aramaki, and K. Yanagisawa, "Continuous system modeling of shape memory alloy (SMA) for control analysis," in *Proc. 5th Int. Symp. Micro Mach. Human Sci.*, 1994, pp. 97–100.
[13] S. Majima, K. Kodama, and T. Hasegawa, "Modeling of shape memory alloy actuator and tracking control system with the model," *IEEE Trans. Control Syst. Technol.*, vol. 9, no. 1, pp. 54–59, Jan. 2001.
[14] Y. Bernard, E. Mendes, and F. Bouillault, "Dynamic hysteresis modeling based on the Preisach model," *IEEE Trans. Magn.*, vol. 38, no. 3, pp. 885–888, Mar. 2002.
[15] D. Hughes and J. Wen, "Preisach modeling of piezoceramic and shape memory alloy hysteresis," in *Proc. 4th IEEE Conf. Control Appl.*, 1995, pp. 1086–1091.
[16] M. Tharayil and A. Alleyne, "Modeling and control for smart mesoflap aeroelastic control," *IEEE/ASME Trans. Mechatron.*, vol. 9, no. 2, pp. 30–39, Mar. 2004.
[17] K. Arai, S. Aramaki, and K. Yanagisawa, "Feedback linearization for SMA (shape memory alloy)," in *Proc. 34th SICE Ann. Conf.*, 1995, pp. 1383–1386.
[18] M. Elahinia and H. Ashrafiuon, "Nonlinear control of a shape memory alloy actuated manipulator," *J. Vibr. Acoust.*, vol. 124, pp. 566–575, Oct. 2002.

[19] D. Grant and V. Hayward, "Variable structure control of shape memory alloy actuators," *IEEE Control Syst. Mag.*, vol. 17, no. 6, pp. 80–88, Jun. 1997.

[20] A. Laub, "A Schur method for solving algebraic Riccati equations," *IEEE Trans. Autom. Control*, vol. AC-24, no. 6, pp. 913–921, Dec. 1979.

[21] A. Bhattacharyya, L. Sweeney, and M. Faulkner, "Experimental characterization of free convection during thermal phase transformations in shape memory alloy wires," *Smart Mater. Structures*, vol. 11, pp. 411–422, 2002.

[22] K. Zhou, J. C. Doyle, and K. Glover, *Robust and Optimal Control*. Englewood Cliffs, NJ: Prentice-Hall, 1996.

[23] K. Glover and D. McFarlane, "Robust stabilisation of normalised coprime factor plant descriptions with H_∞ bounded uncertainty," *IEEE Trans. Autom. Control*, vol. 34, no. 8, pp. 821–830, Aug. 1989.

[24] V. Le and M. Safonov, "Rational matrix GCD's and the design of squaring-down compensators—a state-space theory," *IEEE Trans. Autom. Control*, vol. 37, no. 3, pp. 384–392, Mar. 1992.

[25] D. Chowdhury and D. Stauffer, *Principles of Equilibirium Statistical Mechanics*, 1st ed. Weinheim, Germany: Wiley-VCH, 2000.

[26] H. Khalil, *Nonlinear Systems*, 3rd ed. Englewood Cliffs, NJ: Prentice-Hall, 2002.